

# Variable cirrus shading during CSIP IOP 5. I: Effects on the initiation of convection

J. H. Marsham,<sup>a\*</sup> C. J. Morcrette,<sup>b</sup> K. A. Browning,<sup>b</sup> A. M. Blyth,<sup>a</sup> D. J. Parker,<sup>a</sup>  
U. Corsmeier,<sup>c</sup> N. Kalthoff<sup>c</sup> and M. Kohler<sup>c</sup>

<sup>a</sup> University of Leeds, UK

<sup>b</sup> University of Reading, UK

<sup>c</sup> Universität/Forschungszentrum Karlsruhe, Germany

**ABSTRACT:** Observations from the Convective Storm Initiation Project (CSIP) show that on 29 June 2005 (Intensive Observation Period 5) cirrus patches left over from previous thunderstorms reduced surface sensible and latent heat fluxes in the CSIP area. Large-eddy model (LEM) simulations, using moving positive surface-flux anomalies, show that we expect the observed moving gaps in the cirrus cover to significantly aid convective initiation. In these simulations, the timing of the CI is largely determined by the amount of heat added to the boundary layer, but weak convergence at the rear edge of the moving anomalies is also significant.

Meteosat and rain-radar data are combined to determine the position of convective initiation for all 25 trackable showers in the CSIP area. The results are consistent with the LEM simulations, with showers initiating at the rear edge of gaps, at the leading edge of the anvil, or in clear skies, in all but one of the cases. The initiation occurs in relatively clear skies in all but two of the cases, with the exceptions probably linked to orographic effects.

For numerical weather prediction, the case highlights the importance of predicting and assimilating cloud cover. The results show that in the absence of stronger forcings, weak forcings, such as from the observed cirrus shading, can determine the precise location and timing of convective initiation. In such cases, since the effects of shading by cirrus anvils from previous convective storms are relatively unpredictable, this is expected to limit the predictability of the convective initiation. Copyright © 2007 Royal Meteorological Society

**KEY WORDS** cloud shading; nonclassical mesoscale circulation; flux inhomogeneity; convective inhibition

Received 11 December 2006; Revised 24 May 2007; Accepted 31 May 2007

## 1. Introduction

Predicting the precise location and timing of convective storms remains a major challenge for numerical weather-prediction (NWP) models. Although the new generation of non-hydrostatic models, which use grid spacings of the order of one kilometre, can sometimes give reasonable predictions of such storms (e.g. Golding *et al.*, 2005), they cannot consistently forecast them (Clark and Lean, 2006). The Convective Storm Initiation Project (CSIP) (Browning *et al.*, 2006a), which took place in the summer of 2005 in southern England, aims to improve our understanding of the mechanisms that initiate convective storms in the mid-latitude maritime climate of the UK. This understanding can then be used to understand the likely sources of error in high-resolution NWP forecasts, and so improve NWP.

This paper explores the effects of moving cirrus anvils on the convective initiation (CI) observed on 29 June 2005, during CSIP Intensive Observation Period (IOP) 5.

These anvils were generated by storms over France, and then advected over the UK. A number of the showers that developed during IOP 5 did so within the area of southern England where numerous instruments were deployed as part of CSIP (Browning *et al.*, 2006a). A subjective examination of the location of the first appearance of these showers, made during the course of nowcasting for CSIP, suggested that the presence of cirrus shields may have been influencing the locations of CI (Browning *et al.*, 2006b), despite the cirrus moving at approximately  $15 \text{ ms}^{-1}$ .

It is well known that mesoscale spatial variations in fluxes can induce circulations, such as the sea breezes that frequently affect CI in the UK (Bennett *et al.*, 2006). In general, variations in cloud cover, or other parameters such as soil wetness or vegetation, can also induce such circulations (called ‘nonclassical mesoscale circulations’ by Segal and Arritt (1992)).

Segal *et al.* (1986) described idealized two-dimensional simulations of circulations driven by variable cloud cover. The contrast between an extensive clear area (about 80 km across) and an extensive cloudy area was shown to induce a circulation comparable to a sea breeze, when the clouds reduced solar fluxes by 60%. They

\* Correspondence to: J. H. Marsham, Institute for Atmospheric Science, School of Earth and Environment, University of Leeds, Leeds, LS2 9JT, UK. E-mail: jmarsham@env.leeds.ac.uk

noted that even two hours of partial cloud cover can lead to the generation of a circulation that may be of meteorological significance; but all model runs were performed with slower-moving cloud-cover variations than were observed in CSIP IOP 5 ( $1.7 \text{ ms}^{-1}$  compared with approximately  $15 \text{ ms}^{-1}$ ).

Cases of cloud shading affecting CI had been observed previously. Bailey *et al.* (1981) showed that the contrast between two extensive areas of cloudy and clear sky (about 300 km across) appears to have generated a mesoscale circulation, which initiated storms; and McNider *et al.* (1984) showed that a mesoscale circulation driven by cloud-cover variations was responsible for the initiation of a line of thunderstorms in Texas. However, both these cases involved more extensive areas of slower-moving cloud cover than were observed during CSIP IOP 5. Roebber *et al.* (2002) described a case from Oklahoma and Kansas (USA), where a cirrus shield was important in limiting the development of convection and reducing the competition between storms. Their results also suggested that gaps in the moving cirrus cover (diameters of 50 km or more, with speeds of approximately 50 km/h) could be linked to the initiation of convection. However, this effect on CI was not evaluated statistically, and the relative contributions of boundary-layer warming and convergence induced by the gaps were not evaluated.

Section 2 of this paper briefly describes CSIP IOP 5. Section 3 quantifies the observed effects of the cirrus cover on the surface fluxes. Idealized modelling, described in Section 4, is then used to investigate what effects we expect such moving surface-flux anomalies to have on CI. The observed locations of the CI relative to the cirrus clouds are then discussed in Section 5, in the context of these modelling results.

The observed effects of the cirrus shading on the boundary layer are discussed in the second part of this study (Marsham *et al.*, 2007). There, we show that the boundary layer was approximately  $0.8 \text{ g kg}^{-1}$  drier under thick cirrus, and that this cirrus led to the formation of a stable internal layer at the surface, fewer warm moist updraughts, and in some places a decreased boundary-layer height. These effects on the boundary layer are expected to have inhibited CI, thus supporting the conclusions of this paper.

## 2. Synoptic situation and overview of convective initiation in the CSIP area

A mature cyclone was present over the British Isles on 29 June 2005 (Figure 1). The CSIP area, in southern England, was behind (south of) the occluded front associated with this cyclone. Thunderstorms over northwest France at 06:00 UTC generated long-lived cirrus anvils. After the demise of these storms, the orphaned anvils were advected across the Channel, reaching the CSIP area at around 09:00 UTC. From around 10:30 UTC onwards, convective showers initiated over southern England and quickly developed into a series of thunderstorms. These storms merged to form a band of heavy precipitation extending east–west across Britain (Figure 2). As a result of this heavy rain, some flash-flooding occurred in Oxfordshire (approximately 100 km north of Chilbolton).

Figure 3 shows the orphaned cirrus anvils. These appear as blue areas in the satellite images, since they are cold and reflect solar radiation relatively well. The rain-radar data show that no precipitation from these anvils reached the surface. Convective clouds, which appear as unevenly-coloured yellow regions, were also

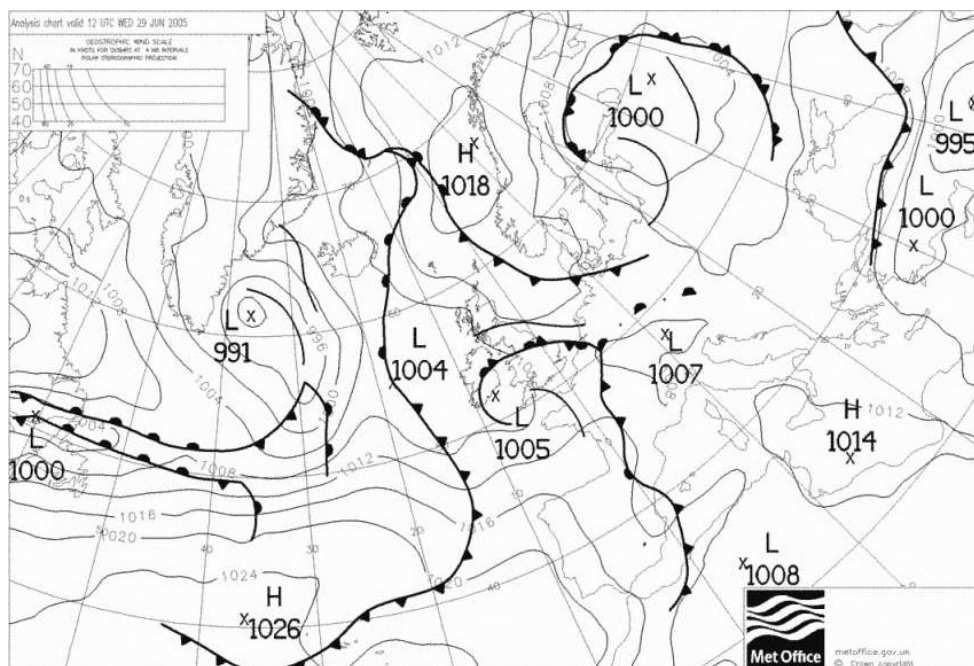


Figure 1. Met Office analysis of mean sea-level pressure at 12:00 UTC on 29 June 2005 (CSIP IOP 5).

observed. Some of these produced significant precipitation, as shown by the rain-radar data. Figure 3 shows a cumulonimbus appearing to form approximately 20 km northeast of Chilbolton on the edge of a roughly-circular gap (diameter about 25 km) at 12:00 UTC. By 13:00 UTC there were two significant showers in this gap, which had grown in size and been advected northwards.

### 3. Observed effects of the cirrus cover on surface fluxes

Figure 4 shows the radiative effects of the cirrus anvils at Chilbolton, where solar and surface fluxes were measured. Surface heat fluxes (Figure 4(a)) were measured by eddy correlation (Andreas *et al.*, 2005; Kalthoff *et al.*, 2006). Figure 4(b) shows visible-wavelength top-of-

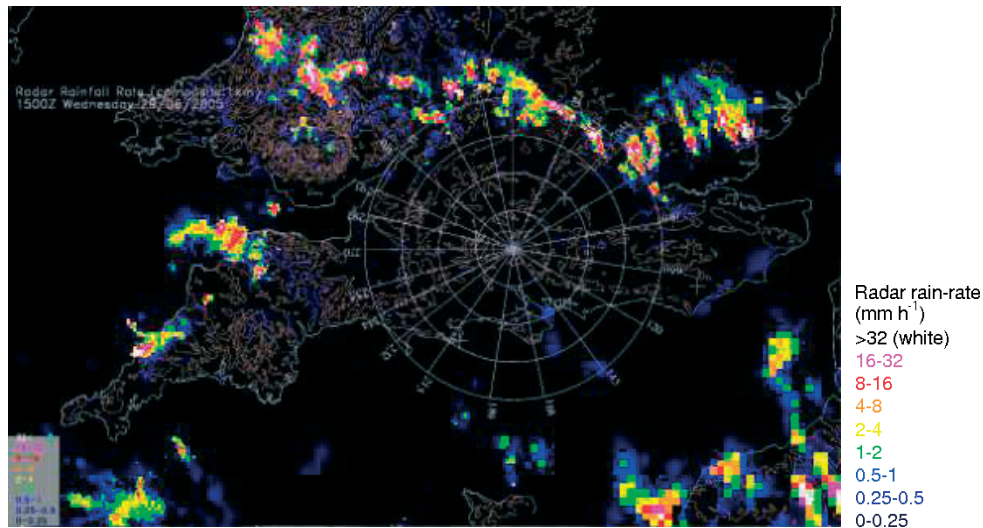


Figure 2. Radar rain rates at 15:00 UTC on 29 June 2005 (CSIP IOP 5). The Chilbolton radar is at the centre of the range rings, shown at 25 km intervals. Part of the line of storms approximately 100 km north of Chilbolton developed from showers that initiated near Chilbolton, which are the subject of this study.

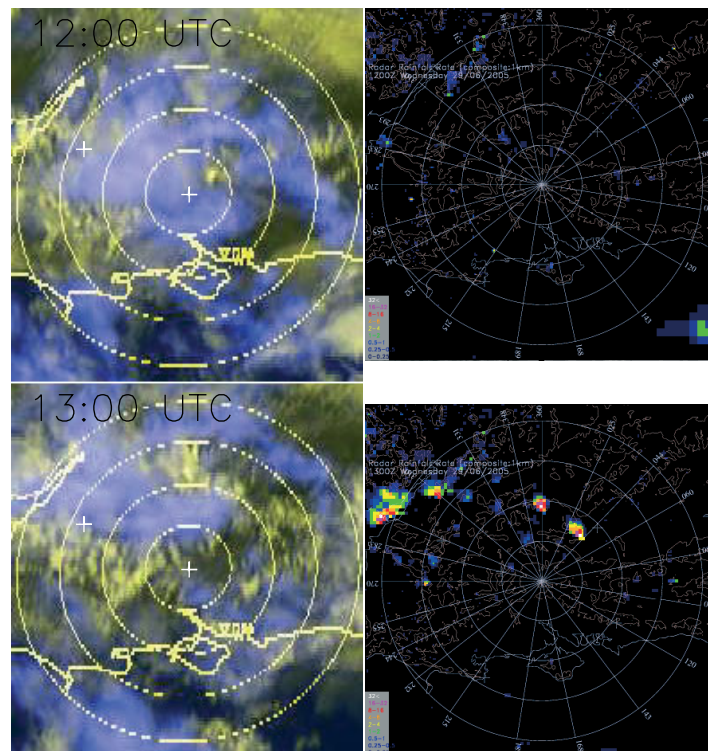


Figure 3. Left: false-colour Meteosat images. Visible top-of-atmosphere reflectance is shown in red and green, and  $11\ \mu\text{m}$  brightness temperature is shown in blue, so that cirrus appears blue and cumulus yellow. Positions of surface-flux observations are indicated by white crosses (with Bath west of Chilbolton). Right: rain-radar data (the colour scale is the same as in Figure 2). Both Meteosat and radar plots are shown at 12:00 and 13:00 UTC, and range rings are centred on the Chilbolton radar and shown at 25 km intervals. The apparent difference between the satellite and radar positions of the easternmost storm at 13:00 UTC is due to parallax.

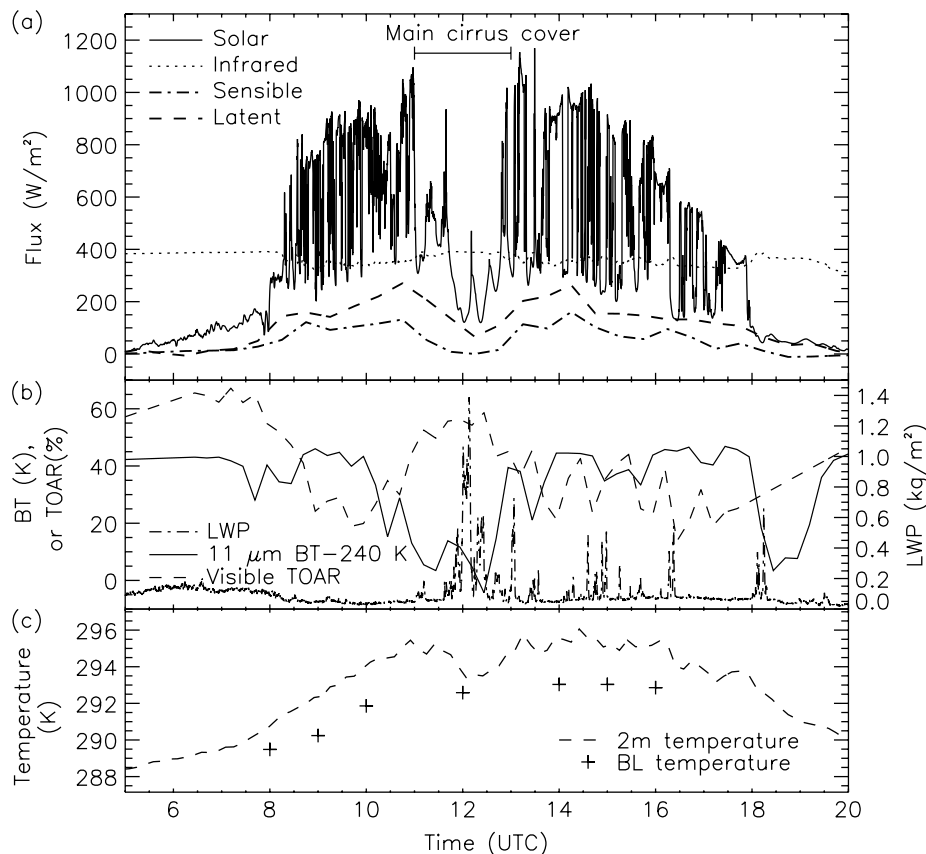


Figure 4. Time series of observations from Chilbolton (with the symbol/line and sampling period shown in brackets): (a) downwelling solar heat flux (solid line, 10 s); downwelling infrared flux (dotted line, 10 s); upward surface sensible and latent heat fluxes (dashed and dash-dotted lines respectively, 15 min). (b) Meteosat observations from the pixel corresponding to Chilbolton: visible TOAR (dashed line, 15 min); infrared BT (solid line, 15 min, with a 240 K offset); liquid-water path (dash-dotted line, 10 s) retrieved from an upwards-pointing dual-wavelength (22 GHz and 28 GHz) microwave radiometer at Chilbolton (Simpson *et al.*, 2002). (c) 2 m air temperature (dashed line, 10 s); boundary-layer potential temperatures from radiosondes averaged over lowest 400 m (crosses, 1 h or 2 h).

atmosphere reflectance (TOAR) and brightness temperature (BT) from Meteosat-8: cirrus clouds give TOARs of 30% or more and low 11  $\mu\text{m}$  BTs, while water clouds give high TOARs and higher BTs.

Figures 4 (a) and (b) show that, between approximately 10:00 UTC and 13:00 UTC, cirrus clouds significantly reduced the incoming solar radiation at Chilbolton, and consequently reduced the upwards sensible heat flux measured at the surface (although Figure 4(b) shows that liquid water added to the effect of the cirrus to give the minimum in observed fluxes at around 12:00 UTC). The cirrus also increased the downwelling infrared flux, although this effect is negligible compared with the effect on the downwelling solar flux. The decrease in surface sensible heat flux caused by the cirrus coverage reduced the strength of the super-adiabatic surface layer, and as a result reduced the difference between the 2 m air temperature and the boundary-layer air temperature (Figure 4(c)). Similar effects were observed at Bath (approximately 65 km west of Chilbolton, as shown in Figure 3), where the cirrus reduced the incoming solar fluxes between about 11:00 and 13:30 UTC (not shown).

The surface-flux variations associated with the cirrus in the CSIP area can be estimated using the observed linear correlations between the downwelling solar heat

flux measured at the surface and the surface sensible and latent heat fluxes (Figure 5). By extrapolation from the data shown in Figure 5, at Chilbolton at 12:00 UTC the clear-sky solar irradiance of approximately  $1100 \text{ W m}^{-2}$  that would have been experienced in the absence of cloud would have given a sensible heat flux of approximately  $210 \text{ W m}^{-2}$ . In reality, at 12:00 UTC cirrus and water clouds reduced the solar flux to approximately  $200 \text{ W m}^{-2}$ , and hence the sensible flux to approximately zero. At around 11:00 UTC, cirrus cover reduced the solar flux to approximately  $400 \text{ W m}^{-2}$ , and hence the sensible flux to approximately  $50 \text{ W m}^{-2}$ . Latent heat fluxes varied linearly with sensible fluxes at both Chilbolton and Bath, and at both sites a zero sensible heat flux still corresponded to a positive latent heat flux (Figure 5). So, given the spatial distribution in downwelling solar radiation, we can estimate spatial distributions of surface sensible flux in the CSIP area, assuming that the surface behaves similarly to that of the flux-measurement sites at Chilbolton or Bath (i.e. flat grass).

Meteosat data were used to estimate the spatial variations in downwelling solar fluxes, and hence to infer surface fluxes. Downwelling solar radiation was measured at the surface at Chilbolton and Bath, as well as on the Dornier 128 aircraft, which was flying at a height

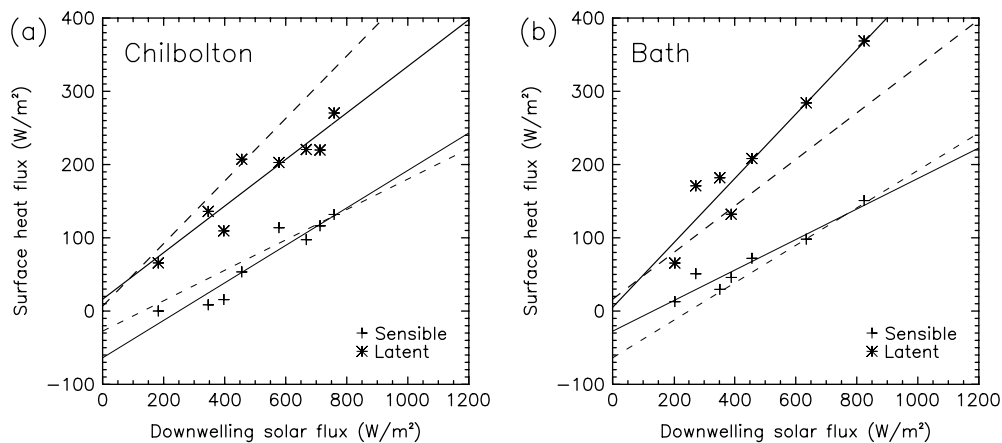


Figure 5. Observed surface and solar fluxes at (a) Chilbolton and (b) Bath, from 10:00 to 14:00 UTC. Solid lines show least-squares fits to data from the named site. Dashed lines show fits to data from the other site.

of about 500 m from 09:00 to 12:38 UTC. The expected clear-sky downwelling solar flux was calculated at hourly intervals using the observed profile and the Fu–Liou radiation code (Fu and Liou, 1992, 1993), and these data were then interpolated to give a value for each observation time.

Figure 6 shows the correlations between the solar transmission (i.e. the observed downwelling solar radiation divided by the calculated clear-sky value) and the Meteosat data, for the visible TOARs and the  $11\ \mu\text{m}$  BTs. (Observed errors in the geolocation of the Meteosat data were corrected, and a parallax correction was applied to all pixels (Johnson *et al.*, 1994), using a cloud-top height of 6 km. This height was derived from vertical scans by the high-power radars at Chilbolton. The Meteosat pixel used was then shifted by up to one pixel north or south to give the best correlations, to allow for uncertainties in these two corrections.) The linear fits calculated for the two sites were similar, except where an outlying observation with a high TOAR gave a shallower gradient for the Bath data.

Figure 7 shows surface sensible heat fluxes calculated from Meteosat data, using the linear fits between Meteosat data and solar transmission (Figure 6), and between surface sensible heat flux and downwelling solar radiation (Figure 5), observed at Chilbolton. The Chilbolton site was chosen, rather than Bath, because the precipitating storms studied were nearer to Chilbolton. These estimated fluxes are valid only over land and for surfaces similar to those where the eddy-correlation fluxes were obtained (i.e. over flat grass). The fluxes are also only valid for cloud conditions similar to those observed. Thus, although Figures 7 (a) and (b) show broadly similar patterns, they do show significantly different fluxes in some areas. Both show extensive areas outside the cirrus coverage (Figure 3) with surface sensible fluxes of approximately  $200\ \text{Wm}^{-2}$ , values of  $0\text{--}50\ \text{Wm}^{-2}$  under the cirrus, and gaps in the cirrus cover with fluxes of about  $150\ \text{Wm}^{-2}$ . However, significant differences between Figures 7 (a) and (b) do occur, for example 100 km north of Chilbolton, in an area affected

by low stratiform cloud, and 75 km west-southwest of Chilbolton, in an area with widespread shallow cumulus. These occur because the correlations between Meteosat observations and solar transmission were derived largely for cirrus cover. However, coverage of low stratiform cloud was very limited in the area of interest during the hours preceding CI, and we show in Section 4.5 that the effects on modelled CI of neglecting the shading from, and radiative heating of, developing cumulus are relatively small.

It is of interest to compare the magnitude of the variations in surface fluxes induced by the moving cirrus anvils with typical effects of land-use variations on surface fluxes. In southern England, apart from land/sea effects, the largest land-use effects are from urban versus rural areas. Urban areas are expected to increase daytime surface sensible fluxes by up to a factor of two and decrease latent heat fluxes by a factor of between one and six (Thielen *et al.*, 2000). There are, however, no major urban areas in the CSIP area (the largest urban areas have diameters of approximately 15 km). Variations in vegetation are likely to have effects of up to only a factor of 2.5 (Segal and Arritt, 1992), and vegetation variations in southern England also tend to occur on small spatial scales, so have limited potential for significant development of mesoscale circulations. In addition, urban areas and vegetation areas essentially alter only the Bowen ratio, which does not alter the flux of equivalent potential temperature (Betts *et al.*, 1996), while gaps in the cirrus shading increase both sensible and latent fluxes, and so increase the equivalent-potential-temperature flux. However, variations in Bowen ratio, due to variations in surface properties, can result in differences in the dependence of the total surface heat flux (sensible plus latent) on boundary-layer cloud cover. This effect has been neglected; but, as discussed above, the vegetation cover of southern England is relatively uniform.

In conclusion, the magnitudes of the cloud-induced variations in fluxes in this case are probably greater than any urban or vegetation effects. However, in contrast with land-use variations, the observed cloud-induced

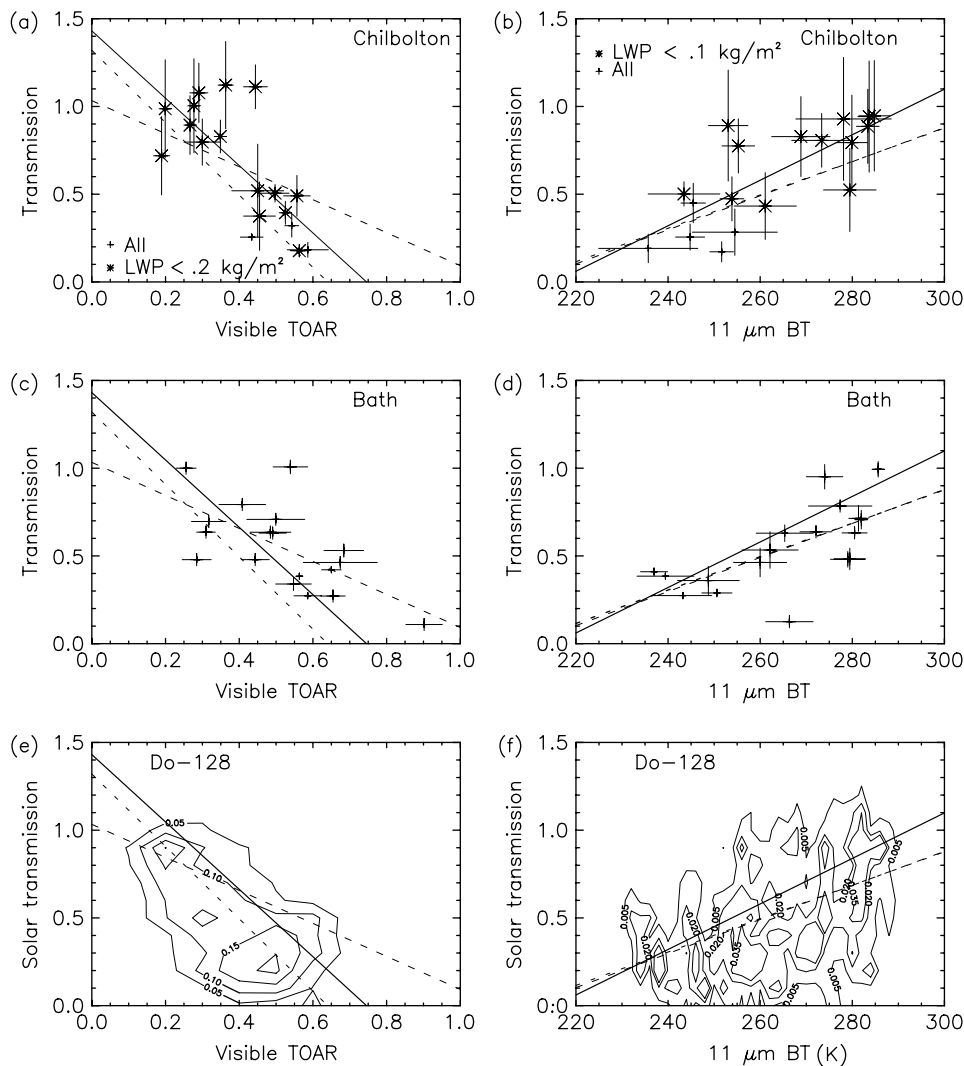


Figure 6. Plots of estimated transmission of solar radiation and Meteosat visible TOAR (a, c, e) and 11  $\mu\text{m}$  BT (b, d, f). Surface data from Chilbolton (a, b) and Bath (c, d) are shown, as well as data from the Dornier 128 aircraft (e, f). For surface data (a, b, c, d), transmission is mean transmission over 200 s (visible) and 600 s (infrared) (i.e. the time taken for a cloud moving at  $5 \text{ m s}^{-1}$  to traverse a Meteosat pixel of 1 km or 3 km). Error bars show the standard deviation in the Meteosat observations over  $3 \times 3$  pixels, and the standard deviation in the solar transmission over 400 s (visible) and 1200 s (infrared) (10 s-resolution data from Chilbolton and 10 min-resolution data from Bath). For aircraft data (e, f), transmission is mean transmission over 10 s (visible) and 30 s (infrared) (i.e. approximately the time taken for the aircraft to traverse a Meteosat pixel of 1 km or 3 km). Straight-line fits are for Chilbolton (solid line), Bath (dashed line), and the aircraft data (dotted line).

variations are moving relative to the surface, and so the effects are short-lived for a given area. The effects of this motion are investigated in the next section.

#### 4. Modelling the effects of moving surface-flux anomalies

Despite the significant approximations in the estimation of effects of the cirrus cloud on the surface fluxes (Figure 7), the estimated fluxes are sufficiently precise for setting up idealized modelling studies, using the Met Office large-eddy model (LEM) (Gray *et al.*, 2001; e.g. Grabowski *et al.*, 2006). These modelling studies test the sensitivity of modelled CI to flux variations of similar magnitudes to those observed during CSIP IOP 5.

The various model runs used are summarized in Table I. Runs using moving positive surface-flux anomalies (POS2D and POS3D) were used to investigate the role of gaps in the cirrus cover in CI. Runs using a moving negative surface-flux anomaly (NEG2D) were used to investigate the development of convection along the outer edges of the cirrus anvil. Finally, runs with a radiative-transfer scheme coupled to the LEM (FULLRADN) were used to investigate the effects of neglecting the shading by convective clouds and the radiative heating of those clouds.

##### 4.1. Method

Simulations using version 2.3 of the LEM were used to simulate the effects of moving surface-flux anomalies. The LEM is a non-hydrostatic model that can be run in one, two or three dimensions. Although the LEM can be used with a three-phase microphysics scheme,

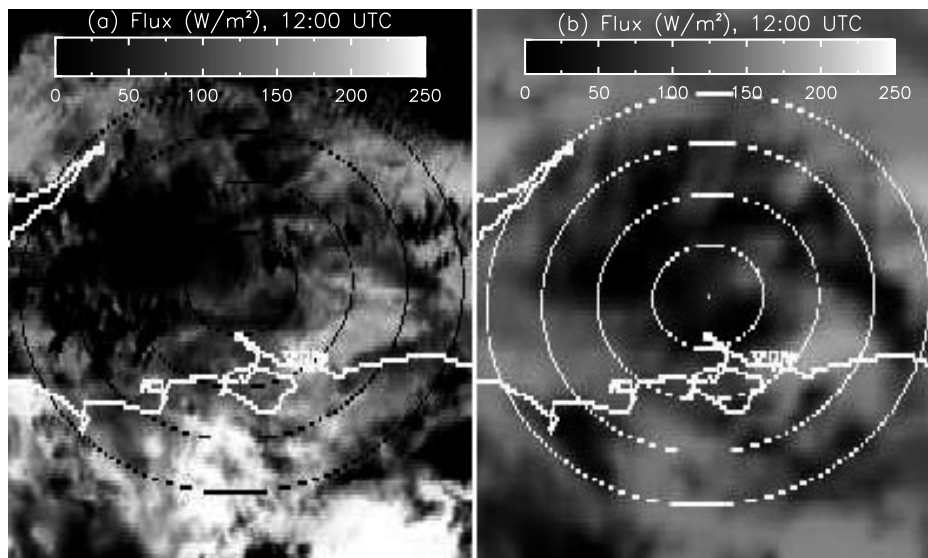


Figure 7. Estimated surface sensible heat flux at 12:00 UTC, calculated using the observed correlation between solar and sensible fluxes (Figure 5), and the mean correlation between solar transmission and (a) Meteosat visible TOAR and (b) Meteosat 11  $\mu\text{m}$  BT (Figure 6). These fluxes were derived using surface-flux observations from two locations, and so errors are large in some areas; fluxes are not valid over the sea.

Table I. Summary of sets of model runs used in this paper.

Name	Domain size	Unperturbed fluxes (sensible & latent, $\text{Wm}^{-2}$ )	$M$	$D$ (km)	$v$ ( $\text{ms}^{-1}$ )
POS2D	500 km	60 & 180	2 to 5	2 to 50	0 to 15
POS3D	500 km by $3 \times D$	60 & 180	5	30	10 and 15
NEG2D	500 km	240 & 480	0.25 to 0.5	100	0 to 15
FULLRADN	500 km	$f$ (solar): see Figure 5	0.5	30	10

only cloud-water and rain (a Kessler rain scheme) were included, since the process of CI that was being investigated occurred before the ice-phase processes were significant (the melting level was at approximately 3000 m, about 1400 m above the level of free convection). The model domain was 20 km deep, and Rayleigh damping was applied above 13 km. For two-dimensional simulations, we used horizontal grid spacings of 200 m and vertical grid spacings of 50–100 m in the boundary layer and 100 m up to heights of approximately 5000 m, with progressively larger vertical grid spacings above 5000 m. Horizontal grid spacings of 1 km were used in three-dimensional simulations (POS3D), because of computational constraints, and vertical grid spacings were identical to those used in two-dimensional simulations. Periodic lateral boundary conditions were used in all simulations.

The model was initialized with the radiosonde sounding, shown in Figure 8, made from Reading at 11:15 UTC. Reading, approximately 50 km northeast of Chilbolton, was the closest site to the initiation of the deeper cells observed northeast of Chilbolton between 12:00 and 13:00 UTC. For two-dimensional simulations, the model domain was aligned with the observed wind at the level of the cirrus clouds. This gave boundary-layer winds of up to  $5 \text{ ms}^{-1}$  (Figure 8(b)).

In all runs, it was assumed that the only effect of the cirrus was to modify the downwelling solar radiation at the surface, and hence the surface fluxes; this is justified, because vertical scans by the Chilbolton radars show that the cirrus did not extend much below 5 km and falling ice could not reach convective storms initiating at around 1600 m (the level of free convection). Radiative heating of the cloud and atmosphere, as well as shading of the surface by the developing convection, were also neglected in most simulations (POS2D, POS3D and NEG2D). These last assumptions were tested in a third set of simulations (FULLRADN), which used a radiative-transfer scheme coupled to the LEM.

For runs used to investigate the role of gaps in the cirrus cover in CI (POS2D and POS3D), uniform sensible and latent fluxes of  $60 \text{ Wm}^{-2}$  and  $180 \text{ Wm}^{-2}$  respectively were applied at the surface in the model, except in the moving flux anomaly, where fluxes were multiplied by a factor  $M$ . This positive flux anomaly represented the effect of a gap in the cirrus cover. The width of the flux anomaly,  $D$ , was varied between 2 km and 50 km. This range of scales encompasses the 25 km size of the gap observed northeast of Chilbolton at 12:00 UTC (Figure 3). The speed of the anomaly was varied between zero and  $15 \text{ ms}^{-1}$ ; the speed of travel of the anvil was tracked by Meteosat (this is consistent with radiosonde

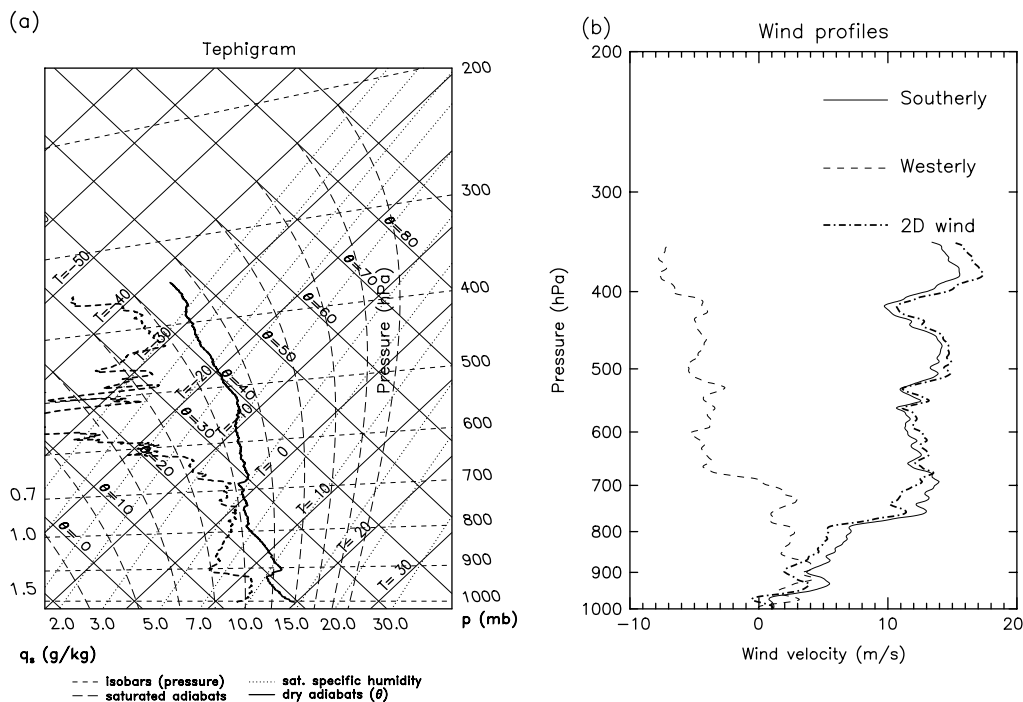


Figure 8. 11:15 UTC radiosonde profile from Reading, one of the nearest radiosonde sites to the early shower-initiation events: (a) tephigram; (b) wind velocities. In the legend, '2D wind' refers to the wind profile used in two-dimensional LEM simulations (this is the wind velocity in the direction of the wind velocity at the cirrus altitude).

wind data, which showed wind speeds of approximately  $15 \text{ ms}^{-1}$  at the cirrus altitude of approximately 7 km, or 400 hPa). The factor  $M$  was varied between 2 and 5. In the two-dimensional simulations, a large domain of 500 km was used. Thus, an anomaly of width 50 km moving at  $15 \text{ ms}^{-1}$  did not reach the far end of the domain in a 7 h simulation. In three-dimensional simulations (POS3D), the domain width was three times the anomaly diameter  $D$  (in the dimension perpendicular to the cirrus steering velocity), and again 500 km long.

To investigate the development of cumulus along the outer edges of the overall cirrus anvil (NEG2D), uniform sensible and latent fluxes of  $240 \text{ W m}^{-2}$  and  $480 \text{ W m}^{-2}$  respectively were applied at the surface in the model, except in the moving flux anomaly where fluxes were reduced by a factor  $M$ . The diameter of the cold anomaly was fixed at 100 km, approximately the diameter of the anvil shown in Figure 3, and its speed again varied between zero and  $15 \text{ ms}^{-1}$ . The model domain was 600 km long. Thus, these experiments were very similar to the positive-anomaly runs, except that in this case the positive area (i.e. the area not affected by the negative anomaly) was wide (500 km), whereas the warm area in the runs with a positive anomaly was narrow (2–50 km).

For the third set of runs (FULLRADN), used to test the assumption that shading by convective clouds and radiative heating of convective clouds could be neglected, a constant top-of-atmosphere downwelling solar flux was used, calculated for 12:00 UTC at Chilbolton on 29 June 2005. This downwelling flux was halved, except in a 30 km gap moving at  $10 \text{ ms}^{-1}$ , which represented the gap in the cirrus cloud cover. The surface fluxes were

specified to depend on the downwelling solar radiation at the surface, using the linear correlation shown for Chilbolton in Figure 5, allowing shading by convective clouds to be accounted for. The four-stream radiation model, with six solar and twelve infrared bands, of (Fu and Liou, 1992, 1993) was used, with an independent pixel approximation.

#### 4.2. Scale analysis

With spatially-uniform and time-invariant surface fluxes, the time taken for cloud top to reach a particular height between 1100 m and 3000 m was found to be, to a good approximation, inversely proportional to the surface flux (not shown). So, with a surface flux  $F$ , the time taken in the absence of a flux anomaly is

$$t = \frac{Q}{F}, \quad (1)$$

where  $Q$  is the amount of heat required per unit area. A moving surface-flux anomaly, with diameter  $D$  and speed  $v$ , increasing surface fluxes by a factor  $M$ , will affect any point for a time less than or equal to  $D/v$ . Therefore, if heat is not mixed horizontally, the time taken for the cloud top to reach a particular height will be reduced by  $(M - 1)D/v$ , if this time depends only on the maximum amount of heat added to the boundary layer at any point.

The situation is not one-dimensional, though. Figure 9 shows a schematic of the heat added to the boundary layer, if the heat is not mixed horizontally, at time  $t > D/v$ . Using this simple model, we expect the pressure perturbation  $\Delta p$  induced by the flux anomaly to

be proportional to  $Q_2 - Q_1$  (Figure 9). Thus, using the Boussinesq approximation, the maximum pressure gradient induced,  $dp/dx$ , is approximated by

$$\frac{\Delta p}{\Delta x} \approx \frac{g}{C_p T} \frac{Q_2 - Q_1}{D}, \quad (2)$$

where  $g$  is the acceleration due to gravity,  $C_p$  is the specific heat capacity of the air, and  $T$  is the mean temperature in the boundary layer. Substituting for  $Q_1$  and  $Q_2$  (Figure 9) gives:

$$\frac{\Delta p}{\Delta x} \approx \frac{g}{C_p T} \frac{(M - 1)F}{v}. \quad (3)$$

These expressions are equally valid for a positive or a negative anomaly, and the pressure gradient is independent of the anomaly diameter  $D$ . From the momentum equation, using

$$\Delta u \approx \frac{1}{\rho} \Delta t \frac{\Delta p}{\Delta x}, \quad (4)$$

(where  $\rho$  is the air density and  $\Delta u$  is the velocity perturbation in time  $\Delta t$ ), and

$$\Delta t = \frac{D}{v},$$

Equation (3) gives:

$$\frac{\Delta u}{\Delta x} \approx \frac{g}{\rho C_p T} \frac{(M - 1)F}{v^2}. \quad (5)$$

Hence, from continuity and convergence in two dimensions,

$$\frac{dw}{dz} = -\frac{du}{dx},$$

we get:

$$\frac{w}{H} \approx \frac{g}{\rho C_p T} \frac{(M - 1)F}{v^2}, \quad (6)$$

where  $w$  is the vertical velocity and  $H$  the depth of the boundary layer. We expect this convergence to be

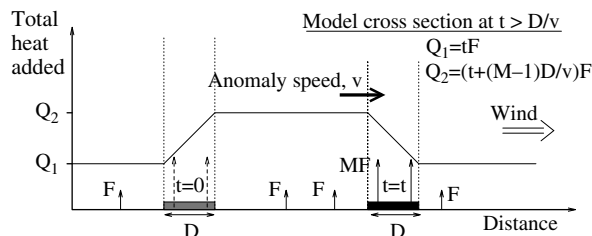


Figure 9. Schematic of the model set-up for the POS2D and POS3D runs, with a positive flux anomaly (diameter  $D$ , speed  $v$ ) at time  $t > D/v$ . The initial anomaly position is shown in grey, and the final position in black. A quantity of heat  $Q_1$  has been added to columns unaffected by the flux anomaly, while for columns over which the whole anomaly has moved, this is increased to  $Q_2$ .

increased for a circular anomaly in three dimensions, using

$$\frac{dw}{dz} = -\frac{du}{dx} - \frac{dv}{dy},$$

in the three-dimensional case.

This uplift will lift any lid at the top of the boundary layer, reducing the convective inhibition (CIN):

$$CIN = \frac{1}{z_0} \int R \Delta T dz, \quad (7)$$

where  $\Delta T$  is the difference in density temperature between the parcel and its surroundings,  $R$  is the gas constant for dry air, and  $z_0$  is the scale height of the atmosphere. Assuming that the convergence leads to adiabatic uplift of air at the top of the boundary layer, this gives:

$$\frac{dCIN}{dt} = \frac{R}{z_0} \left( \frac{p_0}{p} \right)^{-\frac{R}{C_p}} \int w \frac{d\theta_v}{dz} dz, \quad (8)$$

where  $d\theta/dz$  is the dry adiabatic lapse rate, and where we have assumed that pressure is constant over the region of CIN. Over the time  $(D/v)$  for which the anomaly increases the surface fluxes at a point, this will reduce the CIN by approximately

$$\Delta CIN \approx \left( \frac{p_0}{p} \right)^{-\frac{R}{C_p}} \frac{RgH^2}{z_0 \rho C_p T} \frac{d\theta_v}{dz} \frac{(M - 1)FD}{v^3}. \quad (9)$$

Thus, with a flux of  $MF$  over the anomaly, and a constant pressure  $p_0$ , the time taken for CI is reduced by

$$\Delta t \approx \frac{RgH^3}{z_0 C_p T} \frac{d\theta_v}{dz} \frac{(M - 1)D}{Mv^3}, \quad (10)$$

if the whole boundary-layer depth has to be heated to overcome the CIN.

Figure 10 shows another schematic of the heat added to the boundary layer, this time with  $t < D/v$ , again assuming that heat does not mix horizontally. In this case the maximum pressure gradient induced is given by:

$$\frac{\Delta p}{\Delta x} \approx \frac{g}{C_p T} \frac{Q_2 - Q_1}{tv}, \quad (11)$$

or:

$$\frac{\Delta p}{\Delta x} \approx \frac{g}{C_p T} \frac{(M - 1)F}{v}. \quad (12)$$

Using Equation (4), and

$$\Delta x = v \Delta t,$$

we obtain:

$$\frac{\Delta u}{\Delta x} \approx \frac{g}{\rho C_p T} \frac{(M - 1)F}{v^2}. \quad (13)$$

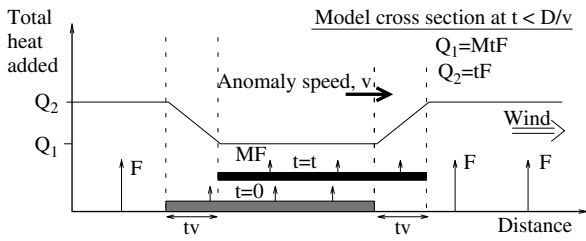


Figure 10. As Figure 9, but for  $t < D/v$  and for a negative flux anomaly (NEG2D).

This is the same expression as Equation (5), for  $t > D/v$ , and again it is valid for positive or negative flux anomalies.

4.3. Modelled effects of moving positive surface-flux anomalies

All runs described in this section are two-dimensional except where stated otherwise. In runs using small (2–50 km-width) positive flux anomalies (i.e. POS2D and POS3D in Table I), the modelled cloud-top height tended to remain at approximately 1 km for some time, and then grew rapidly through the level of free convection at 1600 m to approximately 4 km.

For cases where the time taken for the cloud-top to reach a particular height (the ‘onset time’) is greater than

the transit time ( $D/v$ ), if the one-dimensional argument presented in Section 4.2 holds, then the data shown in Figure 11 should follow straight lines (as indicated by the diagonal dashed lines). The data in Figure 11 are close to straight lines, but with slightly steeper gradients than the 1 : 1 dashed lines shown. This shows that it is largely the quantity of heat added to any point that determines when the cloud top reaches a particular height (the one-dimensional assumption), but the convergence produced by the moving anomalies also significantly aids the development of the convection. The data shown in Figures 11 (b) and (c) are further from the dashed straight lines shown than the data shown in Figure 11(a). This shows that convergence effects are more significant for the time taken for the cloud top to reach 1600 m or 3000 m than 1100 m. The level of free convection is approximately 1600 m, so Figure 11(b) shows the timing of CI. There is a discontinuity in the data shown in Figure 11(b), with CI approximately 1 h faster for  $(M - 1)D/v > 0.7$ . This does not seem to correspond to any threshold in the quantities  $D$ ,  $D/v$ ,  $M$  and so on, but suggests that there is a threshold in  $(M - 1)D/v$  for the anomalies to induce sufficient convergence to affect the modelled CI.

As (Petch, 2006) leads us to expect, increasing the grid spacing from 200 m to 1 km in the Met Office LEM increases the time taken for the cloud top to reach its level of free convection (Figures 11 (b) and (d)). Petch

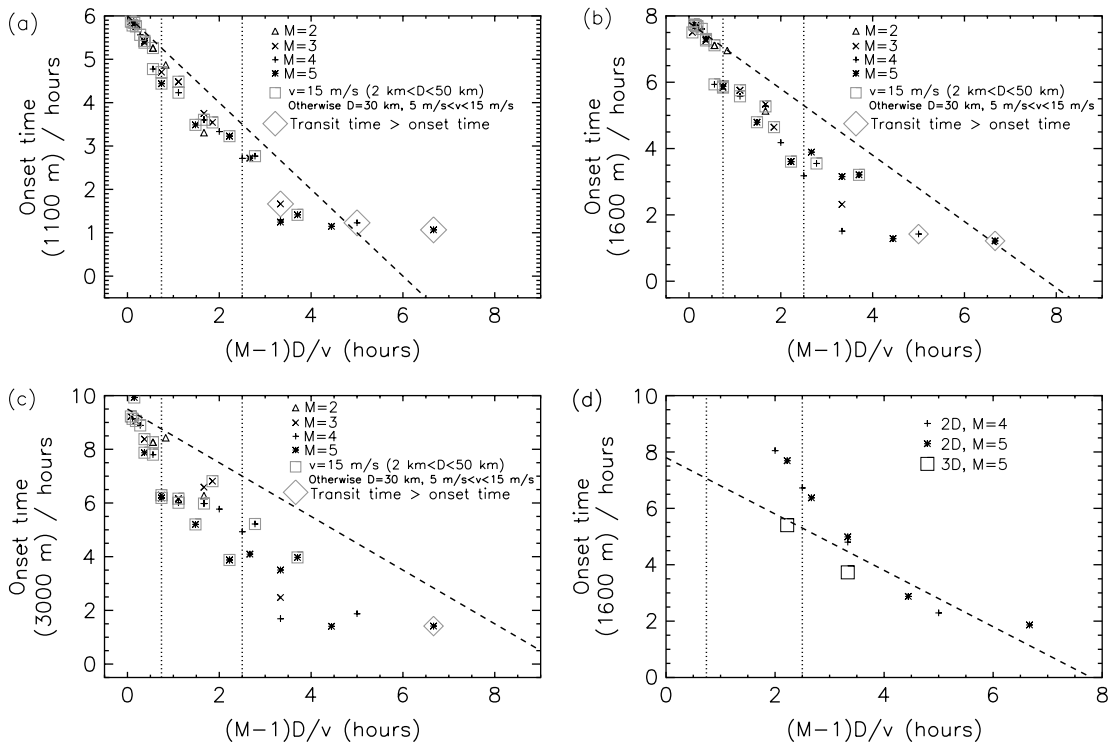


Figure 11. Time taken for cloud-top height to reach (a) 1100 m, (b, d) 1600 m and (c) 3000 m (‘onset time’), plotted against  $(M - 1)D/v$  (the effect of the positive flux anomaly expected from a one-dimensional argument, Section 4.2), for multiple model runs. Panels (a, b, c) show results from two-dimensional runs with 200 m grid spacings. Panel (d) shows results from two- and three-dimensional runs with 1 km grid spacings. Dashed diagonal lines show the results expected from the one-dimensional argument (Section 4.2), with the dashed diagonal line in (d) the same as that shown in (b). Symbols indicate the magnitude of the flux anomaly. Data within a square are for  $v = 15 \text{ ms}^{-1}$  and varying  $D$ ; otherwise data are for  $D = 30 \text{ km}$  and varying  $v$ . Large diamonds indicate where the transit time ( $D/v$ ) is greater than the onset time. Dotted vertical lines demarcate the estimated range of observed  $(M - 1)D/v$ .

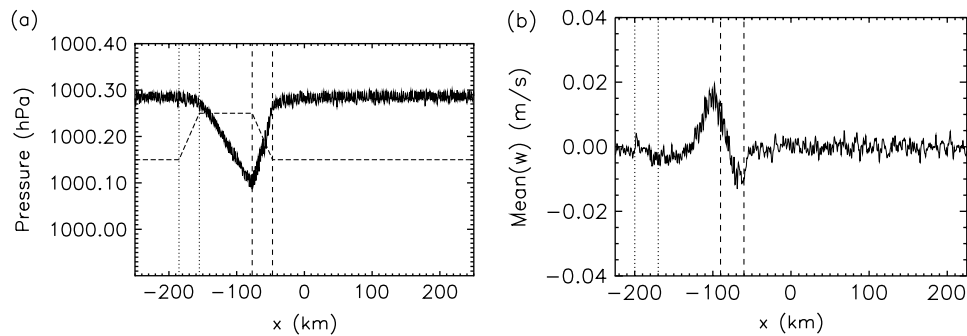


Figure 12. Model cross sections at 3 h (before CI occurs), for a run with a 30 km-diameter positive flux anomaly ( $M = 4$ ) moving at  $10 \text{ ms}^{-1}$ . The anomaly magnitude was increased from  $M = 1$  to  $M = 4$  over the first 2 h of the simulation. (a) Surface pressure is shown by the solid line. The vertical dash-dotted lines show the initial and final positions of the positive surface-flux anomaly. The dash-dotted line from left to right schematically indicates the heat added to each column. (b) As (a), but the solid line shows the horizontally-smoothed vertical velocity averaged over the boundary-layer depth.

(2006) also shows that for simulations with spatially-uniform surface fluxes the development of convection tends to be slower in three dimensions than in two dimensions. However, in this case the use of three dimensions decreases the time required for CI, compared with the two-dimensional case (Figure 11(d)), and this is likely to be from the increased effects of convergence in three dimensions (Section 4.2).

The observations suggest that gaps in the cirrus with diameters of 20–30 km and moving at  $10\text{--}15 \text{ ms}^{-1}$  increased surface fluxes from  $50 \text{ Wm}^{-2}$  to  $150\text{--}200 \text{ Wm}^{-2}$  (Figure 7). Using these ranges of observed values gives:

$$0.74 \text{ h} < \frac{(M - 1)D}{v} < 2.5 \text{ h},$$

(as indicated by the vertical dotted lines in Figure 11(b)). In the two-dimensional LEM simulations, this allowed CI after approximately 3.5–6 h, rather than the 8 h associated with a very weak flux anomaly. Thus the LEM results show that the gaps in the cirrus cover observed during IOP 5 are expected to have significantly aided CI.

Figure 12(a) shows that the pressure perturbation at any point reflects the amount of heat added to the column. For a moving flux anomaly, the pressure perturbation slowly returns towards the unperturbed value behind the anomaly. The minimum pressure is located at the rear edge of the anomaly (Figure 12(a)), and convergence occurs there. This results in uplift in the boundary layer at, or just behind, the rear edge of the moving anomaly, and subsidence at its leading edge (Figure 12(b)).

The position of CI can be understood in terms of the amount of heat added to the boundary layer and the location of the boundary-layer convergence. For a stationary positive flux anomaly and no mean wind, the convection was initiated directly over the positive flux anomaly, as expected. With a mean wind, the convection was initiated towards the downwind side of the anomaly (not shown). If the flux anomaly is moving at  $10\text{--}15 \text{ ms}^{-1}$ , the clouds tend to deepen at the rear edge of the anomaly or behind it (e.g. Figure 13).

Figure 13 also shows that there is a minimum in the modelled boundary-layer depth over the anomaly, and the boundary layer at the rear edge of the anomaly is approximately 200–300 m deeper than in the areas downwind (i.e. larger  $x$ ) that are so far unaffected by the anomaly. Subsidence at the leading edge of the anomaly leads to the lowered boundary-layer depth observed over the anomaly, and the increased heat fluxes and convergence from the anomaly lead to the increased boundary-layer depth at its rear edge (Figure 12); as a result, the modelled CI occurs there. If the anomaly moves at approximately the same speed as the low-level wind, then the convergence is towards the centre of the anomaly, and the clouds deepen here first. With no wind at low levels, the CI again occurs towards the rear edge of the moving flux anomaly (not shown).

Figure 14(a) shows that the pressure gradient induced across the positive flux anomaly is approximately proportional to  $(M - 1)/v$ , consistent with Equation (3), but

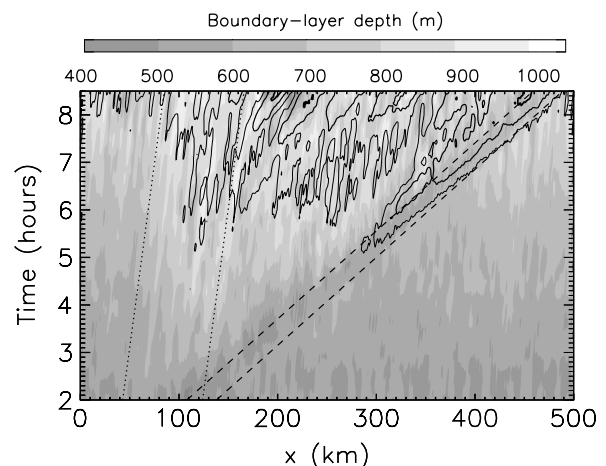


Figure 13. Hovmöller (distance–time) plot of smoothed boundary-layer depth (shaded, 100 m contour interval) and smoothed cloud-top height (contours at 1100 m, 1600 m and 3000 m), using a positive surface-flux anomaly moving at  $15 \text{ ms}^{-1}$ . Dashed lines show the track of the positive flux anomaly. The anomaly magnitude was increased from  $M = 1$  to  $M = 4$  over the 2 h spin-up period. Dotted lines show estimated tracks of boundary-layer features formed at the leading edge of the anomaly at the start and end of the spin-up period.

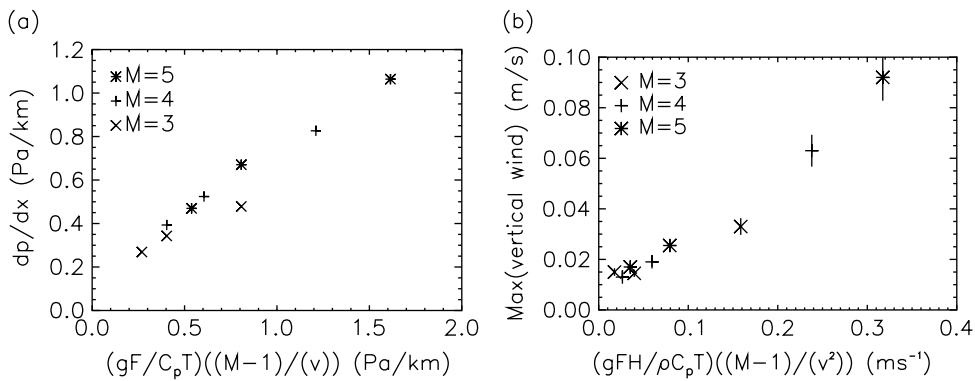


Figure 14. Modelled (a) pressure gradient as a function of  $(M - 1)/v$  (Equation (3)), and (b) maximum vertical velocity integrated over the boundary-layer depth (smoothed over 2 km) as a function of  $(M - 1)/v^2$  (Equation (6)) at 4 h, for runs with no saturation.

the values are approximately three-quarters of those predicted. Figure 14(b) shows the maximum vertical wind in the boundary layer at the rear edge of the positive flux anomaly, which is proportional to  $(M - 1)/v^2$ , consistent with Equation (6), but with values approximately one-third of those predicted. Considering the idealized nature of the arguments used to derive the theoretical values, these differences between the modelled and predicted quantities shown in Figure 14 are not surprising.

Figure 15 shows the difference between the model results and the linear fit shown in Figure 11, as a function of  $(M - 1)D/Mv^3$  (Equation (10)), representing the impact on CIN. The results correlate to some extent, providing some support for the effects of the convergence-driven uplift outlined in Section 4.2. Again, the scatter and the differences in the absolute values are certainly not surprising, given the idealized nature of the scaling arguments involved. The relationship is not as good as that between the deviation and  $(M - 1)D/v$ , however (Figure 11(b)); thus this deviation depends more on the extra heat added to any column by the flux anomaly than on the estimated impact on CIN (Equation (10)). This shows that although the theory outlined in Section 4.2 predicts the pressure gradients and uplift well, the effects on CIN and CI are more complex.

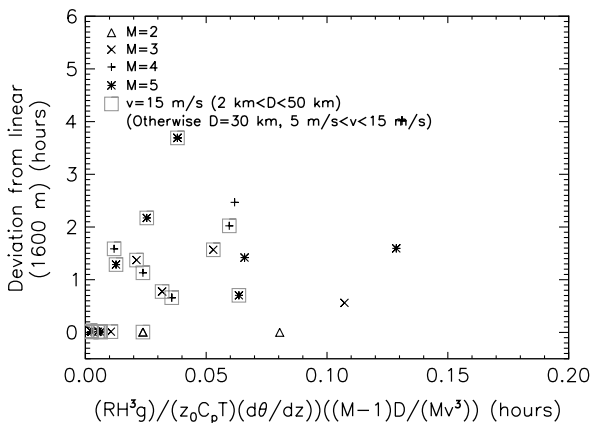


Figure 15. Deviation of data shown in Figure 11(b) from the straight-line fit, as a function of  $(M - 1)D/Mv^3$  (compare with Equation (10)).

#### 4.4. Modelled effects of moving negative surface-flux anomalies

A wide (100 km-diameter) moving negative flux anomaly was applied to represent the effects of the overall cirrus anvil (NEG2D runs, Table I), rather than the positive anomalies used to represent the gaps in Section 4.3. These simulations are essentially similar to those described in (Segal *et al.*, 1986), except that the speed of the cloudy region is much larger here (up to 15 ms<sup>-1</sup> compared with 1.7 ms<sup>-1</sup>). Results from (Segal *et al.*, 1986) suggest that convergence and uplift should be generated at the edges of the cold anomaly, and that this uplift should be maintained or enhanced at the leading edge of the anomaly, but reduced on its trailing edge.

Two sets of simulations were performed. The first included no saturation, so vertical velocities were due to dry convection influenced by the moving cold anomaly. This allowed the effects of the cold anomaly, once it had moved far from its starting position, to be understood without the added complexities of moist convection. In the second, warm phase, microphysics were included. This resulted in clouds forming while the position of the cold anomaly overlapped its initial position.

Figure 16 shows that without saturation in the model the moving cold anomaly suppressed convection in its path, as expected, but there is uplift just inside its leading edge and subsidence at its trailing edge. This uplift is reduced when the anomaly speed is increased (Figure 16(b)), and the uplift and corresponding horizontal pressure gradients are again predicted reasonably well by the theory described in Section 4.1 (not shown).

With saturation included in the model, clouds form and deepen in the region of maximum heating, i.e. ahead of and behind the track of the cold anomaly (Figure 17). Figure 17(a) shows that with a mean wind, which allows clouds to move more ‘in phase’ with the anomaly, deeper convection persists in the region of convergence along the leading edge of the anomaly. Clouds are suppressed in the subsidence at the trailing edge of the moving anomaly, with or without the mean wind in the model (Figure 17).

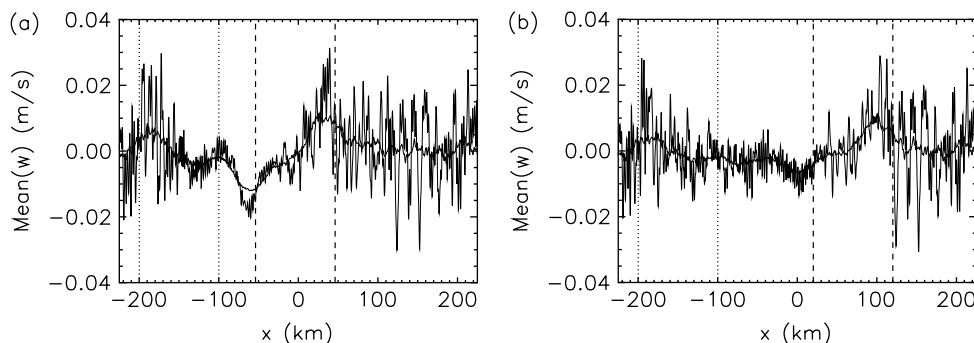


Figure 16. Vertical velocity  $w$ , averaged over the boundary-layer depth after 4 h (so that  $t > D/v$ ), in model runs without saturation and liquid water. The thin and thick lines shows data smoothed over 4 km and 40 km, respectively. Results are from a dry run (i.e. with no saturation), so clouds do not affect the velocities. The observed wind was used. Dotted (dashed) lines give the starting (final) position of the cold anomaly, which is moving at  $15 \text{ ms}^{-1}$ . Anomaly speeds of (a)  $10 \text{ ms}^{-1}$  and (b)  $15 \text{ ms}^{-1}$  were used.

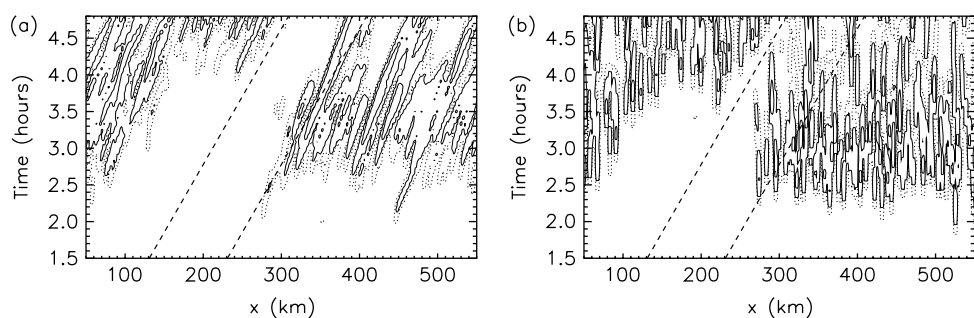


Figure 17. Hovmöller (distance–time) plots of modelled LWP using a cold anomaly, moving at  $15 \text{ ms}^{-1}$ , using (a) observed wind and (b) no wind. Contours are at  $0.01 \text{ kg m}^{-2}$  (dotted lines),  $0.1 \text{ kg m}^{-2}$  (thin solid lines) and  $1.0 \text{ kg m}^{-2}$  (thick solid lines). Dashed lines show the path of the moving cold anomaly.

Overall, the suppression of convection by the cold anomaly is clear, and the results predict enhancement of convection at the leading edge of the cirrus anvils during CSIP IOP 5 and subsidence at their trailing edge. This suggests that the cumulus convection observed at the leading edge of the anvil (Section 5) may have been enhanced by circulations induced by the cirrus-cloud shading.

#### 4.5. Results from simulations using a radiative-transfer model

Here we test the assumptions used so far: that the effects of shading by convective clouds and radiative heating of convective clouds can be neglected. Figure 18 shows a space–time diagram of cloud-top height from model runs (FULLRADN in Table I) neglecting and including these effects. It can be seen that the convection is fairly insensitive to allowing the convective clouds to interact with the downwelling radiation. With and without the fully-coupled radiation, convection develops along the rear (upwind) edge of the positive flux anomaly and behind the anomaly (Figure 18). This justifies the assumption, used in Sections 4.3 and 4.4, that the effects of the cirrus clouds can be represented by moving surface-flux anomalies.

The shading by developing convective clouds reduced the surface sensible heat fluxes by around  $20 \text{ Wm}^{-2}$ . However, radiative heating of those clouds to some extent compensated for the reduction in surface fluxes by increasing the column-integrated radiative heating rates by up to  $10 \text{ Wm}^{-2}$ . These values are small compared with the magnitude of the effects of the solar flux anomaly itself, which in these runs increases surface-sensible-heat fluxes from approximately  $40 \text{ Wm}^{-2}$  to  $125 \text{ Wm}^{-2}$ . As a result, a run allowing for shading by convective clouds and radiative heating of those clouds gives very similar CI to a run neglecting both effects (Figure 18).

### 5. Analysis of observed convective initiation in the CSIP area

Section 2 shows the kind of observational data that led Browning *et al.* (2006a) to hypothesize that variable shadowing by moving cirrus anvils may have affected CI during CSIP IOP 5. Modelling results discussed in Section 4 show that this is indeed to be expected. In this section, we examine the observational data in detail, to see whether these findings are fully substantiated. In fact, the observed fields of cirrus cloud cover and convective development were complex, and so the results,

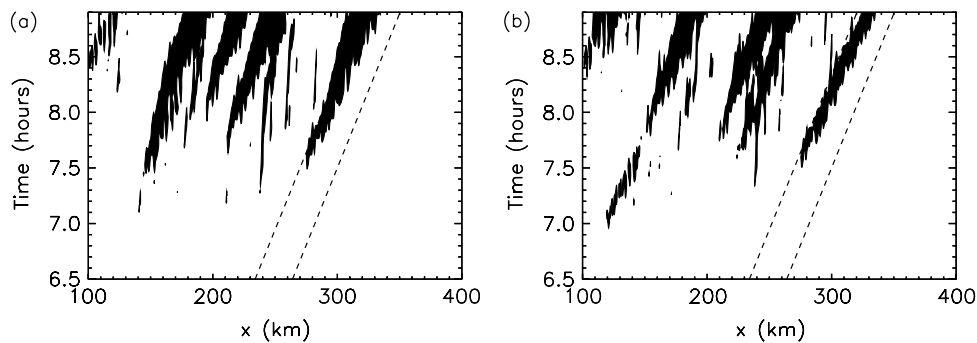


Figure 18. Hovmöller (distance–time) plots of smoothed cloud-top heights above 1600 m, (a) without radiative heating of clouds or shading by convective clouds, and (b) with fully-coupled radiation. The diagonal dashed lines show the path of the moving positive solar flux anomaly, which increased the modelled downwelling solar flux by a factor of two.

while supporting the hypothesis, are not in themselves definitive.

Tracking the observed precipitation and the corresponding cumulus convection, using the rain-radar network and Meteosat data respectively, allowed the locations of convective initiation and development to be determined and compared with the cirrus cloud cover. The starting point of this analysis was to determine the trajectories of all precipitation echoes forming within the CSIP area (a 200 km-by-200 km square centred on Chilbolton) that could be tracked for at least two frames of the 15 min data from the radar network. Those echoes that formed on the outer edge of pre-existing showers, which are likely to have been due to secondary initiation, were excluded from the analysis. A total of 25 showers were tracked in this way.

The high-resolution visible data from Meteosat were then used to track the specific convective clouds associated with these 25 showers. A parallax correction was applied to the Meteosat data (Johnson *et al.*, 1994). This assumed a cloud-top height of 5 km, since radiosonde data collected in the CSIP area showed that, provided the lid at around 900 hPa could be overcome, convection from the surface could rise to a height of around 550 hPa (approximately 5 km). This was also observed in the LEM simulations. Figure 19 shows that there is good agreement between the location of the radar and satellite tracks (black and grey lines, respectively), except that convective clouds were normally visible before precipitation was detected. This shows that the parallax correction used is sufficiently accurate for the purpose intended, i.e. determining the location of the convective clouds with respect to the cirrus clouds.

The 11  $\mu\text{m}$  BT from Meteosat was used to define masks (shown as grey in Figure 19), which approximately described the locations of the cirrus cloud at the times of CI. Observations of the cirrus cloud made by the 3 GHz radar at Chilbolton indicated that the base of the cirrus was located between 5.5 km and 6.5 km. Radiosonde data showed that the temperature at 6 km was around 250 K, so a BT threshold of 250 K was used

to define the area covered by the cirrus clouds. This simple threshold used to define the cirrus mask is fairly crude (for example, it does not take account of thin cirrus that appears warmer than this threshold), but it is useful as a means of classifying the location of initiation of the showers in terms of whether they occur under cloudy or clear sky. In addition, the 250 K threshold used was the maximum BT for which the cirrus shading had clear effects on the water-vapour mixing ratio observed at mid-levels in the boundary layer (Marsham *et al.*, 2007, figure 8).

Determining the location of CI for the clouds that developed into showers was not always easy, because of obscuration by cirrus for certain periods of time, and so the procedure is explained in some detail. For each of the 25 showers, the times of first precipitation echo (FPE) and first satellite cloud were determined from the radar network and Meteosat high-resolution visible data. The observed propagation speeds and directions of the rain showers and cumulus clouds (when detected) were then used to estimate a series of locations for the developing convection in the hour preceding FPE, in case this convection was hidden by cirrus cover during this time. This was not a problem after 13:15 UTC, since after this time all showers initiated in clear skies, so Figure 19 is limited to showing these tracks for showers that formed before this time. If one of these back-trajectory locations had been under the cirrus, then there would have been the possibility that cumulus clouds formed earlier than could be detected and were hidden by the cirrus; but this was never observed to occur. Consequently, for showers for which clouds were detectable in the satellite data, the time of first observed convective cloud was taken as the time of CI. In some cases, however, there were no well-defined clouds in the visible imagery that could be associated with the radar tracks. For these cases, the time of CI was assumed to be the most recent time when the back-trajectory was under clear sky (showers 4, 12, 13 and 19, with assumed CI 30–45 min before FPE). If this never occurred (showers 11 and 17), then initiation must have occurred under the cirrus, and the time of CI was taken as 30 min before FPE (since 32 min was the mean time difference between FPE and observed CI).

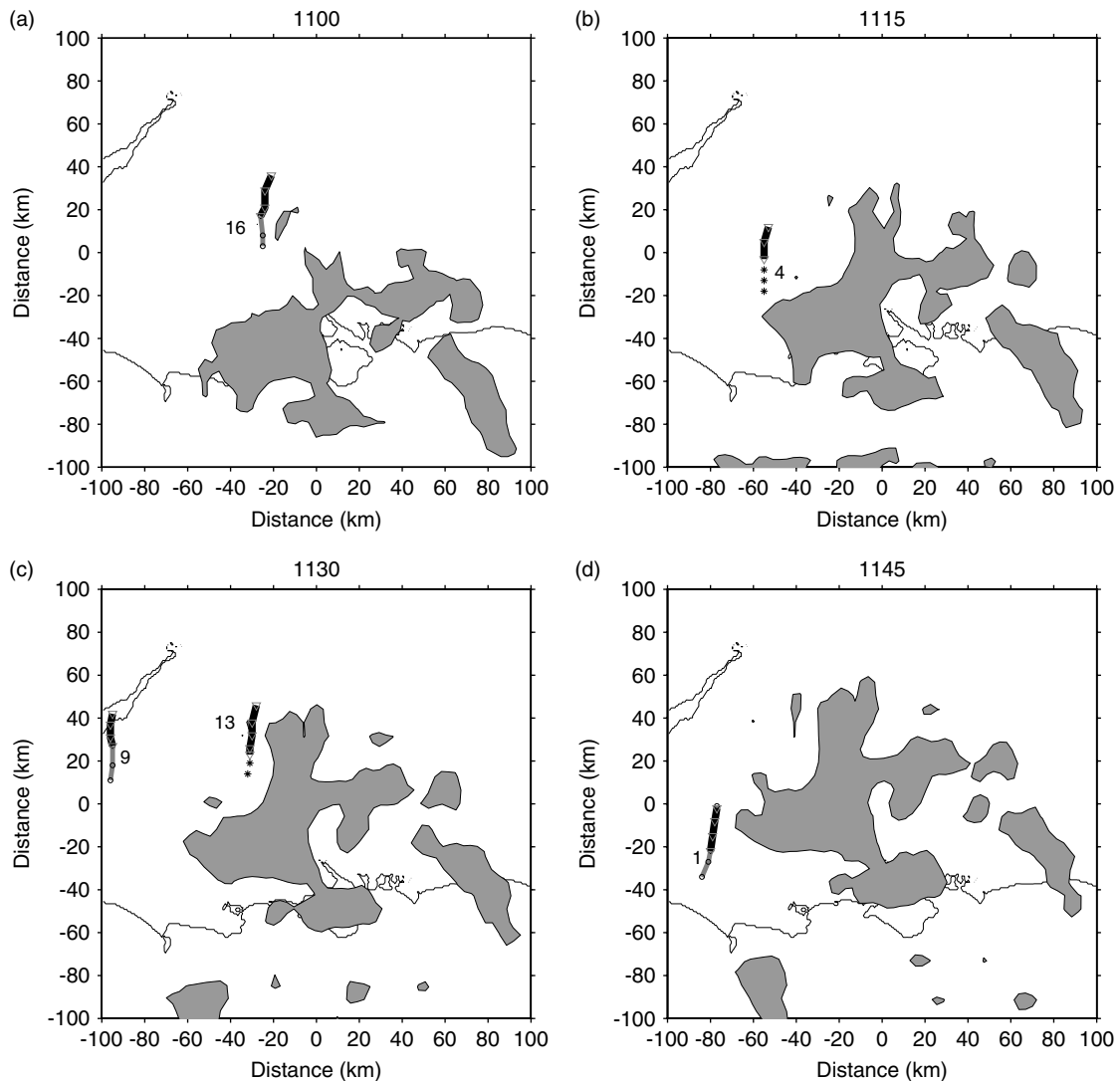


Figure 19. Position of the cirrus mask (grey shading) when CI was estimated to have occurred. The tracks of the showers initiating at that time are plotted using grey triangles and black lines (radar-derived). The tracks of the convective clouds (when seen by Meteosat) are plotted using black circles and grey lines. Inferred locations from CI until a shower was observed are shown by asterisks. The coastline is shown by a black line. Numbers are used to identify each shower. Initiation was observed to occur in clear skies after 13:15 UTC, and so these times are not shown (showers 21 to 25). The figure is continued overleaf.

The above analysis showed 2 out of the 25 showers initiating under the cirrus rather than in clear skies. The mean fraction of sky occupied by the cirrus mask at the times of CI was 14%, so a purely random set of CIs would have had  $3.5 \pm 1.7$  of the 25 showers initiating under the cirrus (1.7 is the standard deviation of the binomial distribution). The observed value of 2 out of 25 is therefore approximately one standard deviation below the mean. Repeating this analysis, but excluding showers forming after 13:15 UTC (since these formed in clear skies) gives an observed value of 2 out of 25 showers, and an expected value of  $2.9 \pm 1.6$  for randomly-distributed showers. These results only allow limited confidence in rejecting the null hypothesis that the cirrus cover did not affect the spatial distribution of the initiation of convection.

Closer inspection of Figure 19 shows that there appear to be four main sub-regions of CI: first, at the leading edge of the anvil (showers 3, 4, 8, 10, 12, 13 and 16);

secondly, within or at the rear edge of the gap in the cirrus that was situated east of Chilbolton at 12:00 UTC (showers 17, 18, 19 and 20); thirdly, in clear skies behind the trailing edge of the cirrus anvil (showers 2, 5, 6, 7, 14, 15 and 21); and finally, in clear skies far from the cirrus (showers 1 and 9, as well as showers 22, 23, 24 and 25, which are not shown but initiated in clear skies after 13:15 UTC). If showers 4, 12, 13 and 19 are assumed to initiate 30 min before FPE, rather than at their last clear-sky location, these categorizations are unchanged. This pattern of behaviour, with observed CI occurring close to the rear edge of gaps, at the leading edge of the cirrus anvil and in clear skies, is consistent with the modelling studies described in Section 4, which show convergence at the leading edge of the anvil and at the rear edge of gaps. Shower 11 is the only clear exception to this pattern, since it initiates under the cirrus anvil (shower 17 initiates under the cirrus, but at the rear edge of a gap).

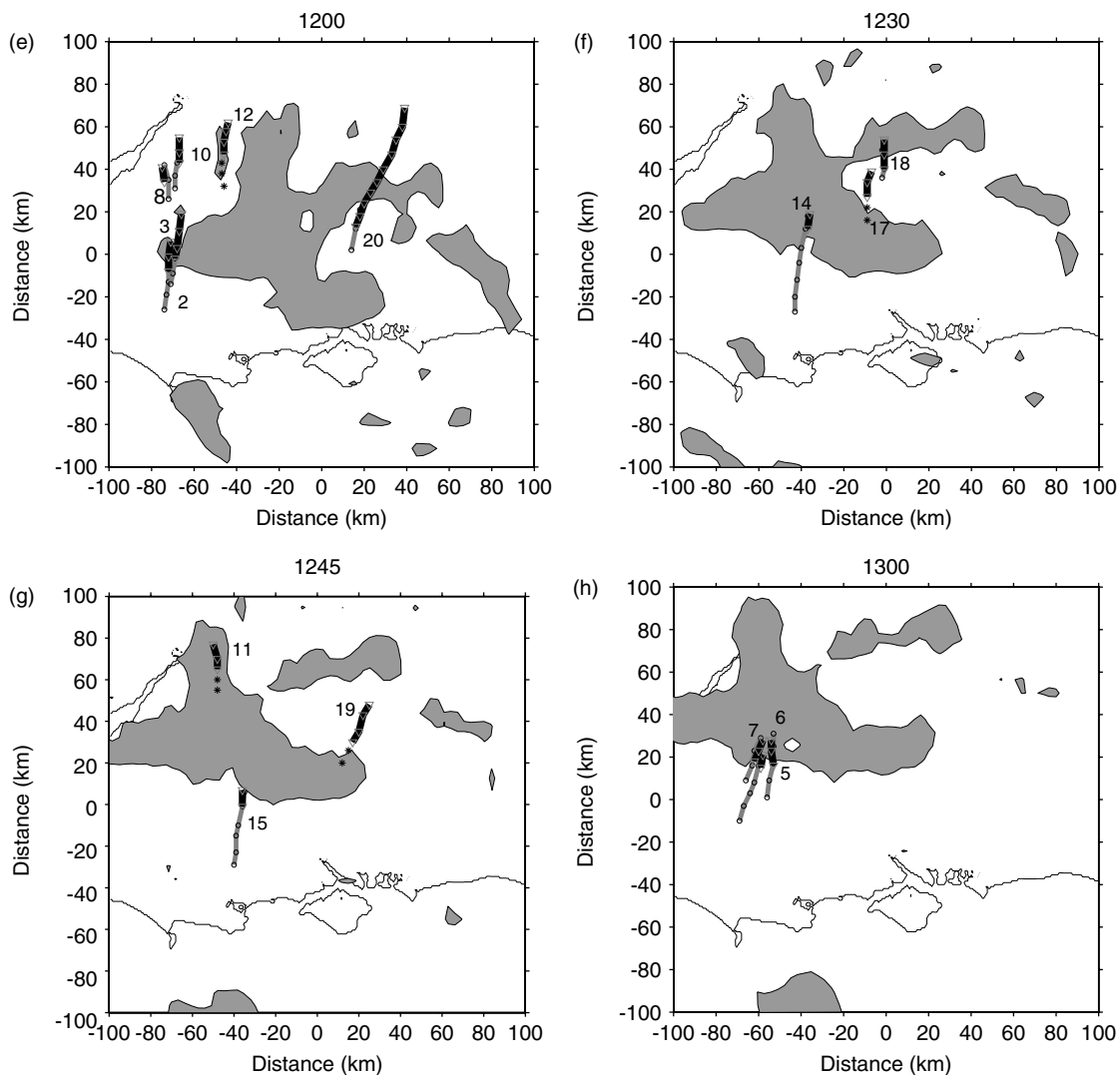


Figure 19. (Continued).

Finally, it is also interesting to note that 6 out of the 25 observed CI locations were within 5 km of the edge of the cirrus mask. If showers were randomly located, we would expect this to be  $1.9 \pm 1.3$  out of 25 (on average, 7.6% of the region was within 5 km of the edge of the mask). Again, repeating this analysis for only showers forming before 13:15 UTC gives an observed value of 6 showers, and an expected value of  $1.6 \pm 1.2$  for randomly-distributed showers. These observed values are significantly larger than those expected from a random distribution of showers, strongly supporting the hypothesis that convergence at the edge of the cirrus anvil affected CI.

Figure 20 shows inferred locations of CI in relation to the orography of the CSIP area. It is clear that showers initiated further south, where the hills also extended further south, suggesting that orographic effects were also significant. Figure 20 also shows that the showers that were inferred to have initiated under the cirrus (11 and 17) formed on the south-facing (windward) slopes of hills, suggesting that orographic effects may have been significant in these cases.

## 6. Conclusions

The results described lead us to believe that shading from cirrus anvils had significant effects on CI during CSIP IOP 5. In LEM simulations, based on observations from IOP 5, cirrus shading suppressed CI, and the rear edge of gaps in the cirrus cover and the leading edge of the cirrus anvil were preferred locations for initiation, because of the convergence there. Observations of CI from rain-radar and Meteosat satellite data support the hypothesis that the leading edge of the anvil, the rear edge of gaps in the cirrus and clear-sky regions were preferred locations for initiation. These results are consistent with (Roebber *et al.*, 2002), but for CSIP IOP 5 the effects of the cirrus shading on surface fluxes have been quantified, LEM simulations have been used to examine the mechanisms, and the observed distribution of initiation events has been evaluated statistically. In addition, the effects of the cirrus shading on the boundary layer, described in (Marsham *et al.*, 2007), provide further support for the hypotheses that variations in cirrus cloud cover led to mesoscale

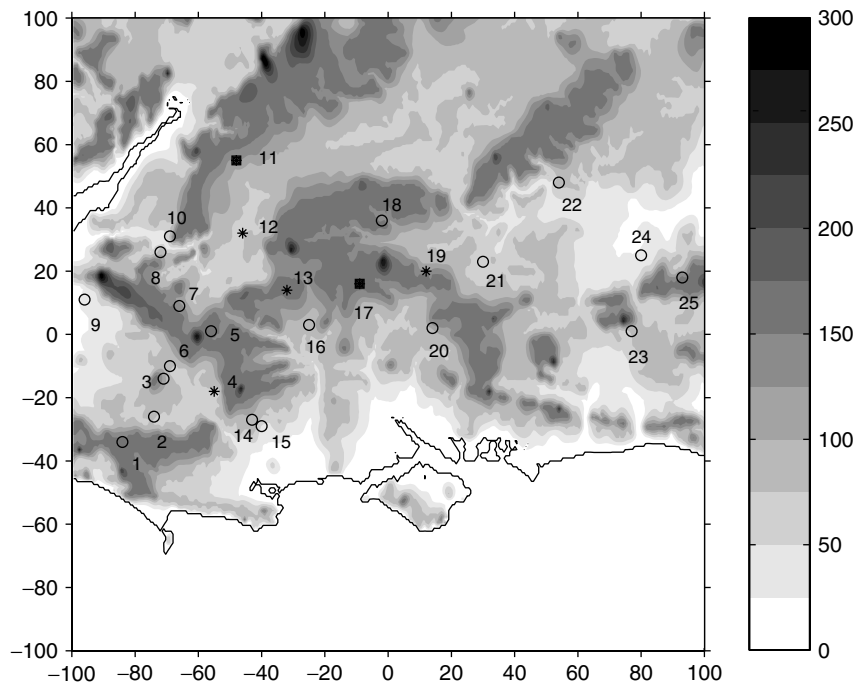


Figure 20. Locations of CI with respect to the height of the orography (m) in the CSIP area. Circles indicates that CI was determined from the appearance of cumulus clouds in clear sky. Asterisks indicate that the location of CI was determined by extrapolating the shower track to the latest time when the track is in clear sky (i.e. initiation occurred in clear sky, but the cirrus then came over and hid the cumuli). Squares indicate that CI occurred under the cirrus and the location had to be inferred.

circulations and that cirrus shading significantly affected CI during CSIP IOP 5.

Observations from Chilbolton showed a nearly-linear variation of surface sensible and latent fluxes with the downwelling solar flux. The cirrus anvils reduced the downwelling solar flux, and so reduced surface fluxes. For thick cirrus, this reduced the surface-sensible-heat flux from the  $200 \text{ Wm}^{-2}$  expected with clear sky to approximately  $0\text{--}50 \text{ Wm}^{-2}$  (Section 3). The effects of shading by the cirrus were represented in the LEM by simply using a moving surface-flux anomaly. Simulations using a radiative-transfer model coupled to the LEM showed that it was reasonable to neglect the shading by, and radiative heating of, convective clouds, since including these effects had little impact on the modelled initiation (Section 4).

Two-dimensional LEM simulations, using a moving positive flux anomaly to represent the effects of a gap in the cirrus cover, were performed. In these runs, the maximum cloud-top height reached a given level slightly sooner than was predicted using a simple model, where the time required depended only on the maximum amount of heat added to any column of the model. This difference increased with increasing cloud-top height, and points to the role of the convergence induced by the moving anomaly in initiating the simulated convection. The pressure gradients and uplift induced by the moving anomalies were shown to be reasonably well predicted by the theory outlined in Section 4.2, which used a Boussinesq approximation and convergence in two dimensions. In addition, three-dimensional runs, performed using a coarser grid spacing, showed that CI occurred more

quickly with three dimensions, and this is likely to be due to increased convergence. The modelled boundary layer was deepest at and behind the rear edge of the moving positive flux anomaly, since the amount of heat added to the boundary layer was greatest behind this edge and the convergence occurred at this edge. As a result, CI tended to occur towards the rear edge of the moving positive flux anomaly (i.e. at the centre of the reduced pressure).

LEM simulations using moving cold surface-flux anomalies to represent the effects of the overall cirrus anvil showed that the cold anomalies suppressed convection in their path, but gave convergence at their leading edges. This convergence was again reasonably well predicted by the theory described in Section 4.2. With a mean wind, which allowed convective clouds to move more in phase with the moving anomaly, deeper convection persisted at the leading edge of the anomaly. Thus, the LEM results, using both the positive and the negative surface-flux anomalies, show that we expect CI at the rear edge of gaps in the cirrus cover and at the leading edge of the cirrus anvil.

A detailed analysis of the locations of CI observed during IOP 5 (Section 5) showed that significantly more CI occurred near the edge of the cirrus than would be expected by chance. This is consistent with convergence effects at the edge of the cirrus cloud, inferred from LEM simulations. The analysis of the observations did not statistically prove or disprove the hypothesis that showers were preferentially initiated in clear skies. However, 24 of the 25 showers observed initiated at the rear edge of gaps in the cirrus, at the leading edge of the cirrus anvil, or in clear skies; this is consistent with the LEM results.

Of the 25 showers, 23 initiated in relatively clear skies, rather than under the cirrus. In both cases, the exceptions initiated over the south-facing slopes of significant hills, suggesting that in these cases orographic effects were significant. In addition, the observed CI occurred further south to the west of Chilbolton, where hills also extend further south, suggesting that the CI may have been more generally affected by the orography.

In summary, this CSIP case shows that for forecasting convective storms using NWP models it is important to predict or assimilate cloud cover and account for its effects on solar and surface fluxes. At the stage of boundary-layer warming when the CIN has become small, very small perturbations can determine precisely where and when CI will occur (e.g. Morcrette *et al.*, 2006; Marsham and Parker, 2006). In such cases, even small gaps in cloud cover, of approximately 30 km diameter, can significantly affect CI, despite moving relative to the surface. NWP models cannot be expected to predict the detailed evolution of upper-level clouds at long lead times, especially for highly inhomogeneous anvils from earlier convective storms. This provides a significant limitation on the predictability of CI in cases where such subtle forcings are significant.

### Acknowledgements

We would like to thank EUMETSAT for the Meteosat data used in this paper, and the Met Office for the Nimrod rain-rate images and the surface-pressure analysis chart used. Observations from Chilbolton were courtesy of the Chilbolton Facility for Atmospheric and Radio Research (CFARR) at the CCLRC-Chilbolton Observatory, distributed via the NERC British Atmospheric Data Centre (BADC). We would also like to thank all those involved in the CSIP field campaigns, and the two anonymous reviewers whose comments have improved the clarity of this paper. This project was funded by the Natural Environment Research Council (NERC): NER/O/S/2002/00971.

### References

- Andreas EL, Jordan RE, Makshtas AP. 2005. Parameterizing turbulent exchange over sea ice: the ice station Weddell results. *Boundary-Layer Meteorol.* **114**: 439–460.
- Bailey MJ, Carpenter LR, Lowther LR. 1981. A mesoscale forecast for 14 August 1975 – the Hampstead storm. *Meteorol. Mag.* **110**: 147–161.
- Bennett LJ, Browning KA, Blyth AM, Parker DJ, Clark PA. 2006. A review of the initiation of precipitating convection in the United Kingdom. *Q. J. R. Meteorol. Soc.* **132**: 1001–1020.
- Betts AK, Ball JH, Beljaars ACM, Miller MJ, Viterbo PA. 1996. The land surface–atmosphere interaction: A review based on observational and global modeling perspectives. *J. Geophys. Res.* **101**: 7209–7225.
- Browning K, Blyth A, Clark P, Corsmeier U, Morcrette C, Agnew J, Bamber D, Barthlott C, Bennett L, Beswick K, Bitter M, Bozier K, Brooks B, Collier C, Cook C, Davies F, Deny B, Engelhardt M, Feuerle T, Forbes R, Gaffard C, Gray M, Hankers R, Hewison T, Huckle R, Kalthoff N, Khodayar S, Kohler M, Kraut S, Kunz M, Ladd D, Lenfant J, Marsham J, McGregor J, Nicol J, Norton E, Parker D, Perry F, Ramatschi M, Ricketts H, Roberts N, Russell A, Schulz H, Slack E, Vaughan G, Waight J, Watson R, Webb A, Wieser A, Zink K. 2006a. The Convective Storm Initiation Project. *Bull. Am. Meteorol. Soc.* (to appear).
- Browning K, Morcrette C, Blyth A, Bennett L, Clark P, Corsmeier U, Agnew J, Barkwith A, Barthlott C, Behrendt A, Bennett A, Beswick K, Bozier K, Brooks B, Chalmers N, Collier C, Cook C, Dacre H, Davies F, Davies L, Davies O, Deny B, Devine G, Dixon M, Engelhardt M, Fitch A, Forbes R, Gaffard C, Gallagher M, Goddard J, Gray M, Hewison T, Huckle R, Illingworth A, Kalthoff N, Keeley S, Khodayar S, Kilburn C, Kohler M, Kottmeier C, Kraut S, Ladd D, Lean H, Lenfant J, Marsham J, McGregor J, Mobbs S, Nicol J, Norton E, Parker D, Perry F, Ramatschi M, Richardson A, Ricketts H, Roberts N, Russell A, Slack E, Vaughan G, Watson R, Webb A, Weckwerth T, Wieser A, Wilson J, Wrench C, Wulfmeyer V, Zink K. 2006b. 'A summary of the Convective Storm Initiation Project Intensive Observation Periods'. Met Office Forecasting Research Technical Report: 474/JCMM Report 153.
- Clark P, Lean H. 2006. 'An overview of high resolution UM performance for CSIP cases'. Met Office Forecasting Research Technical Report: 478/JCMM Report 155.
- Fu Q, Liou KN. 1992. On the correlated  $k$ -distribution method for radiative transfer in nonhomogeneous atmospheres. *J. Atmos. Sci.* **49**(22): 2139–2156.
- Fu Q, Liou KN. 1993. Parameterization of the radiative properties of cirrus clouds. *J. Atmos. Sci.* **50**(13): 2008–2025.
- Golding B, Clark P, May B. 2005. Boscastle flood: Meteorological analysis of the conditions leading to the flooding on 16 August 2004. *Weather* **60**(8): 230–235.
- Grabowski WW, Bechtold P, Cheng A, Forbes R, Hailliwell C, Khairoutdinov M, Lang S, Nasuno T, Petch J, Tao WK, Wong R, Wu X, Xu KM. 2006. Daytime convective development over land: A model intercomparison based on LBA observations. *Q. J. R. Meteorol. Soc.* **132**: 317–344.
- Gray MEB, Petch J, Derbyshire SH, Brown AR, Lock AP, Swann HA. 2001. 'Version 2.3 of the Met. Office large eddy model'. Met Office (APR) Turbulence and Diffusion Rep. 276. Met Office, Exeter, UK.
- Johnson DB, Flament P, Bernstein RL. 1994. High-resolution satellite imagery for mesoscale meteorological studies. *Bull. Am. Meteorol. Soc.* **75**: 5–33.
- Kalthoff N, Fiebig-Wittmaack M, Meißner C, Kohler M, Uriarte M, Bischoff-Gauß I, Gonzales E. 2006. The energy balance, evapotranspiration and nocturnal dew deposition of an arid valley in the Andes. *J. Arid Environ.* **65**: 420–443.
- Marsham JH, Parker DJ. 2006. Secondary initiation of multiple bands of cumulonimbus over southern Britain. II: Dynamics of secondary initiation. *Q. J. R. Meteorol. Soc.* **132**: 1053–1072.
- Marsham JH, Blyth AM, Parker DJ, Beswick K, Browning KA, Corsmeier U, Kalthoff N, Khodayar S, Morcrette CJ, Norton EG. 2007. Variable cirrus shading during CSIP IOP 5. II: Effects on the convective boundary layer. *Q. J. R. Meteorol. Soc.* **133**: 1661–1675.
- McNider RT, Jedlovec JD, Wilson GS. 1984. Data analysis and model simulation of the initiation of convection on April 24, 1982. Pp. 543–549 in *Tenth Conf. on Weather Forecasting and Analysis*, Tampa. American Meteorological Society.
- Morcrette CJ, Browning KA, Blyth AM, Bozier KE, Clark PA, Ladd D, Norton EG, Pavelin E. 2006. Secondary initiation of multiple bands of cumulonimbus over southern Britain. I: An observational case-study. *Q. J. R. Meteorol. Soc.* **132**: 1021–1051.
- Petch JC. 2006. Sensitivity studies of developing convection in a cloud-resolving model. *Q. J. R. Meteorol. Soc.* **132**: 345–358.
- Roebber PJ, Scultz DM, Romero R. 2002. Synoptic regulation of the 3 May 1999 tornado outbreak. *Weather and Forecasting* **17**: 399–429.
- Segal M, Arritt RW. 1992. Nonclassical mesoscale circulations caused by surface sensible heat-flux gradients. *Bull. Am. Meteorol. Soc.* **73**(10): 1593–1604.
- Segal M, Purdom JFW, Song JL, Pielke RA, Mahrer Y. 1986. Evaluation of cloud shading effects on the generation and modification of mesoscale circulations. *Mon. Weather Rev.* **114**: 1201–1212.
- Simpson PM, Brand EC, Wrench CL. 2002. 'Microwave radiometer measurements at Chilbolton – liquid water path algorithm development and accuracy'. EU\_FP5-CloudNET Project Report.
- Thielen J, Wobrock W, Gadian A, Mestayer PG, Creutin JD. 2000. The possible influence of urban surfaces on rainfall development: a sensitivity study in 2D in the meso- $\gamma$ -scale. *Atmos. Res.* **54**(1): 15–39.